Supporting Information

Photoelectron Spectroscopy of Methide Anion: Electron Affinities of $^{\bullet}CH_3$ and $^{\bullet}CD_3$ and Inversion Splittings of CH_3^- and CD_3^-

Allan M. Oliveira,[†] Yu-Ju Lu,[†,⊥] Julia H. Lehman,[†] P. Bryan Changala,[§] Joshua H. Baraban,[‡,∥] John F. Stanton,[∥] W. Carl Lineberger*[,†]

[†] JILA and Department of Chemistry and Biochemistry, University of Colorado, Boulder, Colorado 80309

[‡] Department of Chemistry and Biochemistry, University of Colorado, Boulder, Colorado 80309

[§] JILA and Department of Physics, University of Colorado, Boulder, Colorado 80309

[∥] Department of Chemistry, University of Texas, Austin, TX 78712

* Correspondence should be addressed to wcl@jila.colorado.edu

Contents

A. Peak assignments and experimental vibrational frequencies of $^{\bullet}CH_3$ and $^{\bullet}CD_3$

As indicated in Section III in the main text, Table S1 shows the assignments of the peaks labeled in Figure 1 and 2. Here, the assignments reflect the electron photodetachment process, where the single and double primes represent vibrational levels in the neutral and anion species, respectively. Table S2 shows the experimentally observed umbrella vibrational frequencies of $^{\bullet}CH_3$ and $^{\bullet}CD_3$ from this work, as well as previous high resolution work. The agreement, where available, between this work and prior work is very good; previously unobserved vibrational frequencies are also reported here. In addition, anharmonicity constants are derived, as discussed in the main text.

Table S1. Experimentally determined electron binding energies of each peak and transition assignments for each peak in the photoelectron spectra of CH_3^- and CD_3^-. Each eBE value corresponds to the center of each individual transition, as determined by fitting the peak to a Gaussian form. The values in parentheses are the uncertainties described in the text.

$^{\bullet}CH_3 + e^- \leftarrow CH_3^-$			$^{\bullet}CD_3 + e^- \leftarrow CD_3^-$		
Peak[a]	electron Binding Energy, eBE (cm^{-1})	Assign. $\nu_2' \leftarrow \nu_2''$	Peak[a]	electron Binding Energy, eBE (cm^{-1})	Assign. $\nu_2' \leftarrow \nu_2''$
a	303(10)	$0 \leftarrow 1^+$	a	294(8)	$0 \leftarrow 1^+$
A	757(9)	$0 \leftarrow 0^+$	A	674(8)	$0 \leftarrow 0^+$
B	1340(5)	$1 \leftarrow 0^-$	B	1128(7)	$1 \leftarrow 0^-$
C	2045(5)	$2 \leftarrow 0^+$	C	1640(7)	$2 \leftarrow 0^+$
D	2755(4)	$3 \leftarrow 0^-$	D	2175(7)	$3 \leftarrow 0^-$
E	3542(6)	$4 \leftarrow 0^+$	E	2748(7)	$4 \leftarrow 0^+$
F	4308(6)	$5 \leftarrow 0^-$	F	3325(5)	$5 \leftarrow 0^-$
G	5157(5)	$6 \leftarrow 0^+$	G	3917(3)	$6 \leftarrow 0^+$
H	5977(4)	$7 \leftarrow 0^-$	H	4545(4)	$7 \leftarrow 0^-$
I	6860(3)	$8 \leftarrow 0^+$	I	5170(3)	$8 \leftarrow 0^+$
[a] Peak labels shown in Figures 1 and 2 of the main text.					

Table S2. Observed umbrella mode (v_2) vibrational frequencies and derived spectroscopic constants of neutral $^{\bullet}CH_3$ and $^{\bullet}CD_3$ (cm^{-1}).

	$^{\bullet}CH_3$		$^{\bullet}CD_3$	
$\nu_2' \leftarrow \nu_2''$	Previous work	This work[d]	Previous work[c]	This work[d]
1 ← 0	606.4531[a]	606(10)	457.8136	460(10)
2 ← 1	681.6369[a]	688(8)	507.9297	510(10)
3 ← 2	731.0757[a]	734(7)	542.2841	542(10)
4 ← 3	772(4)[b]	769(8)	568.6322	570(10)
5 ← 4	811(4)[b]	790(9)		584(8)
6 ← 5		830(8)		588(6)
7 ← 6		845(6)		635(6)
8 ← 7		864(4)		622(6)
Derived Spectroscopic Constants				
ω_2		627(1)[e]		474(2)[e]
x_{22}		18(1)[e]		11(1)[e]
[a]Ref. 1, [b]Ref. 2, [c]Ref. 3				
[d]Values corrected by the inversion splitting. Uncertainties are described in the main text.				
[e]The reported uncertainty is the 1σ statistical error in a quadratic fit of the inversion corrected peak positions as a function of vibrational quantum number.				

B. Photoelectron Angular Distribution

The photoelectron anisotropy parameter is derived for each peak in the vibrational progressions shown in Figures 1 and 2 of the main text. The intensity (number of electron counts) as a function of the angle (θ) with respect to the laser polarization at the radius corresponding to each peak is fit to the form: $I(\theta) \propto \frac{1}{4\pi}(1 + \beta P_2(\cos(\theta)))$, where β is the anisotropy parameter. The error in the resulting β values, shown in Figure S1, comes from the scatter of the measured β values across each peak FWHM.

The β values as a function of photodetached electron kinetic energy (eKE) are fit to the modified Wigner-Bethe-Cooper-Zare equation in the work by Sanov *et al.*[4] that describes the angular anisotropy of electron photodetachment from a mixed *sp* hybrid orbital as a function of electron kinetic energy (ε):

$$\beta(\varepsilon) = \frac{2\,Z\,\varepsilon + 2A\varepsilon^2 - 4\varepsilon\cos(\delta_2 - \delta_0)}{\frac{1}{A} + 2A\varepsilon^2 + Z\,\varepsilon} \quad (1)$$

where

$$Z = \frac{1-f}{f}\frac{B}{A}$$

Here, ε represents the eKE, Z and A and B are parameters whose physical significance is described below, and $\cos(\delta_2 - \delta_0)$ is the relative phase-shift between the outgoing waves of $\Delta l = \pm 1$. The A and B parameters describe the scaling of the radial dipole integrals corresponding to the $l \rightarrow l \pm 1$ (A) and $l \leftrightarrow l - 1$ (B) photodetachment channels. While there are initially four fitting parameters, Sanov shows that for mixing 2*s* and 2*p* hydrogenic orbitals, the ratio B/A becomes 8/3, and $\cos(\delta_2 - \delta_0) \cong 1$, *i.e.,* no phase-shift between the outgoing electron waves, which reduces the number of fitting parameters to two. The parameter f is associated with the relative *p*-character of the initial orbital, where the limiting cases of $f = 0$ and 1 describe pure *s* and *p* orbitals, respectively, according to the following expression for the HOMO of the anion:

$$|\psi\rangle_{HOMO} = \sqrt{1-f}|s\rangle + \sqrt{f}|p\rangle$$

The ratio of the A and B photodetachment channels (now assumed to be 8/3) is included in the fitting equation through the Z parameter, and weighted by the coefficient $(1-f)/f$ for the relative contributions of the *s* and *p* orbitals. More detailed information can be found in papers by Sanov.[4-7]

The β parameters obtained from the experimental data are shown in Figure S1 for the CH_3^- photoelectron spectra using 1.165 eV and 0.383 eV photon energies. In addition, we include here photoelectron spectra taken with 2.33 eV and 1.63 eV photon energies (not shown in the main text). The solid green line in Figure S1 is the best fit of Eq. (1) to the experimental data, resulting in $f = 0.80$ and $A = 1.15$ eV^{-1}. The grey shaded area depicts the sensitivity of the experimental fit as f is varied from 0.7 to 0.9, while A is held constant. The dashed horizontal line at $\beta = 0$ corresponding to an isotropic photoelectron angular distribution at all eKE is shown for clarity. The image inset in Figure S1 shows the calculated HOMO of CH_3^-, which results in $f = 0.89$ (dashed blue curve), consistent with the experimental value. The measurements included in Figure S1 are summarized in Table S3. Very similar results were obtained, as expected, for the CD_3^- isotopologue (not shown).

The anisotropy data show experimental evidence of the sp^3 hybridization of the pyramidal CH_3^- anion. The f factor of 0.80 indicates that the electron is detached from an orbital whose wavefunction has approximately 80% p_z-character and 20% *s*-character. This is very similar to the expected f factor of 0.75 for an sp^3 hybrid orbital. Interestingly, this f factor decreases to 0.74 if the B/A ratio is allowed to vary away from the assumed 8/3. The resulting B/A ratio is then closer to 2, which is similar to the ratio derived for mixing the larger 3*s* and 3*p* hydrogenic orbitals.[6]

The A parameter in Eq. (1) was found to be 1.15 eV^{-1}. Using a hydrogenic orbital radial profile and detachment from a 2*p* orbital, the A factor can be analytically derived as 0.588 eV^{-1}, assuming an effective charge of 1.[6] While this describes detachment from O^- quite well (experimental $A = 0.55 \pm 0.045$ eV^{-1}), there is a noticeable difference between results from this simple model and that of C^- (0.75 eV^{-1}) and now CH_3^- photodetachment as well. Since A is effectively the spatial extent of the anion wavefunction of the HOMO, this discrepancy was previously accounted for by the larger size of C^- compared to O^-.[6] From the theoretical data shown below, it is clear that in order to accurately describe the HOMO of CH_3^-, more diffuse functions must be used. This is completely consistent with the larger A parameter.

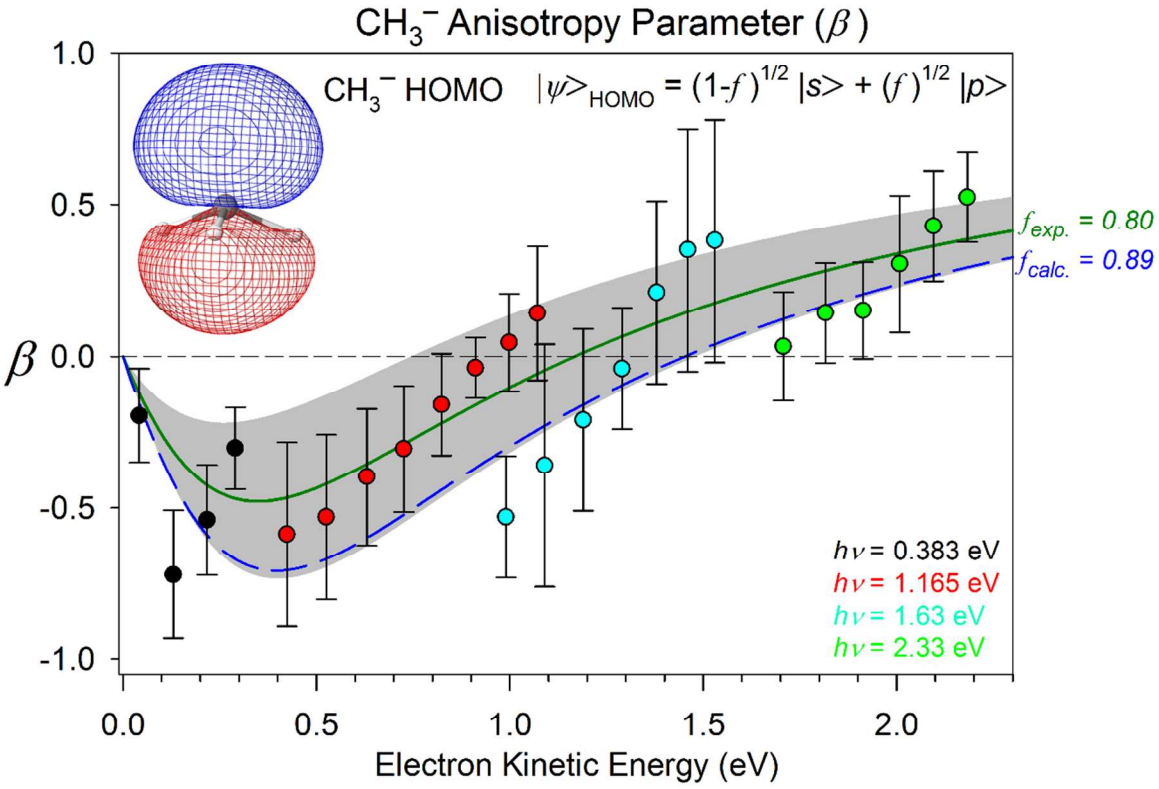

Figure S1: CH_3^- photoelectron anisotropy parameter (β) as a function of electron kinetic energy. The β values (circles) are from the peaks observed in the photoelectron spectra using 0.383 eV (black), 1.165 eV (red), 1.63 eV (blue), and 2.33 eV (green) photon energies. The best fit of Eq. (1) to the experimental data ($f = 0.80$, $A = 1.15$) is shown as the solid green curve and the calculated value from the CH_3^- HOMO ($f = 0.89$) is shown as the blue dashed curve. The grey shaded area shows the sensitivity of the f factor to the fit to the experimental values. Here, the f factor was varied by ±0.1 while keeping A constant.

Table S3: Anisotropy parameter (β) measurements for each peak in the CH_3^- photoelectron spectra used. The values are color coded to match Figure S1.

$CH_3^- \rightarrow {}^{\bullet}CH_3 + e^-$		
eKE (eV)	$\boldsymbol{\beta}$	**Transition** ($\nu_2' \leftarrow \nu_2''$)
2.18	0.5(2)	$1 \leftarrow 0^+$
2.10	0.4(2)	$2 \leftarrow 0^-$
2.01	0.3(2)	$3 \leftarrow 0^+$
1.91	0.2(3)	$4 \leftarrow 0^-$
1.82	0.1(2)	$5 \leftarrow 0^+$
1.71	0.0(1)	$6 \leftarrow 0^-$
1.53	0.4(2)	$0 \leftarrow 0^+$
1.46	0.4(4)	$1 \leftarrow 0^-$
1.38	0.2(3)	$2 \leftarrow 0^+$
1.29	0.0(2)	$3 \leftarrow 0^-$
1.19	-0.2(3)	$4 \leftarrow 0^+$
1.09	-0.4(4)	$5 \leftarrow 0^-$
1.07	0.1(2)	$0 \leftarrow 0^+$
1.00	0.0(2)	$1 \leftarrow 0^-$
0.99	-0.5(4)	$6 \leftarrow 0^+$
0.91	0.0(1)	$2 \leftarrow 0^+$
0.82	-0.2(2)	$3 \leftarrow 0^-$
0.73	-0.3(2)	$4 \leftarrow 0^+$
0.63	-0.4(2)	$5 \leftarrow 0^-$
0.53	-0.5(3)	$6 \leftarrow 0^+$
0.42	-0.6(3)	$7 \leftarrow 0^-$
0.29	-0.3(2)	$0 \leftarrow 0^+$
0.22	-0.5(2)	$1 \leftarrow 0^-$
0.13	-0.7(2)	$2 \leftarrow 0^+$
0.04	-0.2(1)	$3 \leftarrow 0^-$

C. Energy scale calibration and rotational band-origin correction

In order to verify the accuracy of the photoelectron kinetic energy measurements, we compared the ν_2 (v = 0 → v = 4) umbrella mode frequency (2791(4) cm^{-1}) in neutral ${}^{\bullet}CH_3$ from Yamada *et al.* and Hermann *et al.*[8,9] using an energy scale calibration from the O_2 spacing from (v = 0 → v = 4) transition (4598.84 (3) cm^{-1})[10] and *vice-versa*. The vibrational level spacings are consistent within 0.0001 eV (1 cm^{-1}) in O_2 and 0.0005 eV (4 cm^{-1}) in ${}^{\bullet}CH_3$, which confirms that the energy scale uncertainty does not significantly affect the electron kinetic energy measurements.

The spectral resolution in the VMI spectrometer improves as the electron kinetic energy (eKE) decreases While the mid-IR, 3239 nm wavelength can give us the best resolution, the

much higher laser flux available with 1064 nm radiation allows for much less noisy data and also better adjustment of the conditions necessary for a high resolution experiment. For these reasons both spectra are close to equivalent in overall quality. The mid-IR data, however, provides us the most accurate position of the $^{\bullet}CH_3$ (v = 3) peak, and therefore the best calibration of the spacing $^{\bullet}CH_3$ (v = 1 – 3). This is taken into account when we weigh the experimental data to obtain the inversion splitting.

Since the observed peak maxima may not represent the band origin due to unresolved rotational structure in the peak, we use the procedure described by Engelking[11] to obtain the shift of the band origin with respect to the observed peak center. The Engelking model recognizes that rotational selection rules appropriate for a bound-free transition are more complex than for a bound-bound transition; however, the analysis is limited to no change in the J, K populations upon electron detachment and makes a correct argument that the shift contributions by the P and R branches largely offset each other. In this case, the detached electron shows a predominantly isotropic (*i.e.*, *s*-wave) angular distribution. The anion HOMO (sp^3) has largely *p*-orbital character, and implies that the photon angular momentum is largely accounted for by the ejected photoelectron. This observation further strengthens the validity of the Engelking approximation. The approximate rotational shift as a function of rotational temperature derived by Engelking for an oblate symmetric top is:

$$\Delta E \approx k_B T[B'/B'' + C'/2C'' - 3/2] + (B'' - B')/3$$

where ΔE is the offset between peak center and the band-origin, B and C are the rotational constants of the oblate symmetric top. The primed quantities refer to the upper state (neutral) and the double-primed quantities refer to the lower (anion) state. The rotational constants for $^{\bullet}CH_3$ (v = 0 – 3) and $^{\bullet}CD_3$ (v = 0 – 4) are obtained from Yamada *et al.* and Sears *et al.*[8,9] and calculated for CH_3^- and CD_3^- ($v = 0^+, 0^-$), by the methods described in the text. Assuming a rotational temperature of 150 ± 50 K leads to a shift of the origin (EA) peak of 10(4) cm^{-1} (1.2(5) meV) in CH_3^- and of 7(3) cm^{-1} (0.9(4) meV) in CD_3^-.

D. Gas-Phase Acidities at 298 K

The experimental data directly give the acidity of methane at 0 K. In order to obtain the gas-phase acidities at 298 K, we use the thermal correction $H^o_{298K} - H^o_{0K} = \int_0^{298.15} C_p(T)\, dT$ where $C_p(T)$ is the heat-capacity at constant pressure of the individual species. Here, the thermal corrections for CH_4, H^+ and D^+ are obtained from the Active Thermochemical Tables[12] and are non rigid-rotor/anharmonic oscillator values. For CD_4, the thermal correction was obtained from Pamidimukkala *et al.*[13] For CH_3^- and CD_3^-, the heat capacities are calculated from the partition functions of the isolated molecules. Here, the rotational contributions to the partition function are calculated in a rigid-rotor approximation using the calculated rotational constants, while the vibrational contributions are calculated from an explicit sum over the vibrational energy levels of the normal modes. We rely on the measured vibrational frequencies (when available) in conjunction with the calculated frequencies from Table S6. The thermal corrections are summarized in Table S4.

Table S4: Thermal corrections ($H^o_{298K} - H^o_{0K} = \int_0^{298.15} C_p(T)\, dT$) for the individual species in the methane deprotonation thermochemical cycle.

Species	$H^o_{298K} - H^o_{0K}$ (kcal/mol)
CH_3^-	2.554
H^+	1.481
CH_4	2.396
CD_3^-	2.572
D^+	1.481
CD_4	2.473

E. Constrained Potential Energy Surface

The constrained 4D potential energy surface calculation is justified through the use of test calculations on NH_3. Using the AMMPOT4 potential energy surface of NH_3 from Marquardt *et al.*,[14] we computed the umbrella inversion splitting of the ground state and first excited state of the umbrella mode ν_2 to be 0.78 and 33.55 cm^{-1}, respectively, with the 4D approximation. The full dimensional values for this surface are 0.75 and 33.95 cm^{-1}, *i.e.* there is only a few-percent error, which is adequate to the meet the goals of these calculations. It is physically reasonable that this should be the case as the minimum energy isomerization paths for umbrella inversion for both CH_3^- and NH_3 maintain C_{3v} symmetry.

The initial 4D potential energy surface was calculated at the CCSD(T)/d-aug-pVTZ level of theory using the CFOUR quantum chemistry package.[15] On this surface, the energy of the barrier height between the planar transition state and the pyramidal equilibrium geometry minima (E_B) is 555 cm^{-1}. The E_B value is strongly dependent on the use of diffuse basis functions, as might be expected for this system since the extra electron is more weakly bound at the transition state. The effect of diffuse basis functions is shown in the first three rows of Table S5.

Initial vibrational calculations (see below) on the CCSD(T)/d-aug-pVTZ surface yielded ground state inversion splittings approximately one-half the measured values, indicating that the CCSD(T)/d-aug-pVTZ barrier height is probably too high. As detailed in Table S5, this reference value was then corrected for the following effects: 1) triple augmentation, 2) core correlation, 3) higher order excitation terms in the correlation treatment (triples and non-iterative quadruples), and finally 4) extrapolation to the complete basis-set limit (leading to the "Total method/basis-set corrections").

Additional contributions to the inversion barrier height include: 1) the diagonal Born-Oppenheimer correction (DBOC), 2) scalar relativistic effects including one- and two-electron Darwin and mass-velocity terms, and 3) zero point energy associated with degrees of freedom not explicitly included in the 4D model, namely the degenerate bending mode. All corrections described above are shown in Table S5, along with corrections to the electronic contribution to the electron affinity (ΔE_{elec}).

The diagonal Born-Oppenheimer correction (DBOC) arises from the non-separability of the nuclear and electronic degrees of freedom, and tends to be particularly large for molecules containing light nuclei. The DBOCs for $CH_3^-/CH_3^-(TS)/^{\bullet}CH_3$ and $CD_3^-/CD_3^-(TS)/^{\bullet}CD_3$ are:

553/542/540 cm^{-1} and 456/450/450 cm^{-1}, respectively, but largely cancel when we calculate E_B and ΔE_{elec}.

Since the degenerate bending mode (ν_4) is not explicitly included in the 4D electronic potential energy surface calculation, we approximately account for this orthogonal mode by including the change in ZPE of ν_4 between the anion minima and the transition-state. At the CCSD(T)/d-aug-pVTZ level of theory, the harmonic frequency of the degenerate bending mode ν_4 (ω_{bend}) at the transition state (1379 cm^{-1}) is reduced by 38 cm^{-1} relative to its value at the equilibrium geometry (1417 cm^{-1}).

Taking these corrections to be independent, the reported calculated E_B and ΔE_{elec} are obtained by adding all the corrections (which do not include the first line of Table S5) to the initial CCSD(T)/d-aug-pVTZ result (shown bold in Table S5). This results in a calculated best estimate for the barrier height of 386 cm^{-1}, a nearly 25% reduction of the original CCSD(T)/d-aug-pVTZ value of 555 cm^{-1}.

Table S5: Computational results for the CH_3^-/CD_3^- 4D transition state barrier height (E_B) and $^{\bullet}CH_3/^{\bullet}CD_3$ electronic contribution to the electron affinity (ΔE_{elec}). The initial reference calculation at the CCSD(T)/d-aug-pVTZ level of theory, to which the corrections are applied, is shown in bold. All values are given in wavenumbers (cm^{-1}).

Method/basis-set	E_B[a]	$\Delta(E_B)$[b]	ΔE_{elec}[c]	$\Delta(\Delta E_{elec})$[d]
CCSD(T)/aug-pVTZ	972 cm^{-1}	+417 cm^{-1}	-76 cm^{-1}	-255 cm^{-1}
CCSD(T)/d-aug-pVTZ (ref. calc.)	**555**	**0**	**179**	**0**
CCSD(T)/t-aug-pVTZ	503[e]	-52	184	+5
AE-CCSD(T)/d-aug-cc-pCVTZ	537	-18	158	-21
CCSDT(Q)/d-aug-pVTZ	518	-37	253	+74
CCSD(T) basis-set extrapolation[f]	545	-10	375	+196
Total method/basis-set corrections	*438*	*-117*	*433*	*+254*
Further corrections				
DBOC[g]	---	-11/-6	---	-13/-7
Darwin correction[h]	---	+3	---	-4
ω_{bend}(TS) - ω_{bend}(min)	---	-38/-20	---	---
Final Reported Calculation	**386/410**	**---**	**415/421**	**---**

[a] Planar anion transition state 4D barrier height

[b] Difference between E_B at CCSD(T)/d-aug-pVTZ and E_B at this level of calculation.

[c] Difference between anion minimum and neutral minimum (*i.e.* without zero-point energy corrections)

[d] Difference between ΔE_{elec} at CCSD(T)/d-aug-pVTZ and ΔE_{elec} at this level of calculation.

[e] For the anion transition state CCSD(T)/t-aug-pVTZ calculation only, d-aug orbitals were used on the hydrogens, and the energy was calculated at the CCSD(T)/d-aug-pVTZ transition state geometry.

[f] Extrapolation of CCSD(T)/d-aug-pVXZ (X=T,Q,5) values.

[g] Diagonal Born-Oppenheimer correction calculated at SCF/d-aug-pVTZ plus CCSD corrections calculated with an aug-pVTZ basis. The values refer to the CH_3/CD_3 systems respectively.

[h] Calculated with MP2/d-aug-pCVTZ .

Given that the best estimate barrier height is significantly lower than the CCSD(T)/d-aug-pVTZ value (386 cm^{-1}), we construct a scaled potential surface, V_s, in terms of the raw CCSD(T)/d-aug-pVTZ potential energy surface, V_0, as follows:

$$V_s(\vec{q}) = \left[V_0(\vec{q}) - V_0(\vec{r}, \vec{\varphi}_{eq})\right] \times \left(1 - \frac{\Delta_{TS}\theta\left(|\varphi_{eq}| - |\varphi|\right)}{V_0(\vec{q}_{TS}) - V_0(\vec{r}_{TS}, \varphi_{eq})}\right) + V_0(\vec{r}, \varphi_{eq})$$

where $\vec{q} = (\vec{r}, \varphi) = (r_1, r_2, r_3, \varphi)$, Δ_{TS} is the total transition state energy correction (defined as positive when the corrections lower the barrier height), and $\theta(x)$ is the Heaviside step function. The form of this scaling is such that $V_s(\vec{q}_{TS}) = V_0(\vec{q}_{TS}) - \Delta_{TS}$, as desired. The step function ensures that only points with geometries closer to planarity than the equilibrium geometry ($|\varphi| < |\varphi_{eq}|$) are scaled, while the continuity of the surface is maintained. This procedure is validated by the agreement between our calculated and measured values for the inversion splitting, as showed in the main text.

F. Vibrational Energy Calculation

For the CH stretches, we used 20 harmonic oscillator (HO) DVR functions spanning 0.6 to 1.6 Å, and for the inversion angle, we used 50 HO DVR functions spanning φ = –60 to 60 degrees. Eigenenergies and eigenvectors were obtained via a custom thick-restart Lanczos algorithm[16] optimized for the form of our Hamiltonian. The sparse structure of the DVR representation enables efficient evaluation of the Hamiltonian-vector product needed during each Lanczos iteration. Approximately 1000 Lanczos iterations were required to achieve the desired Lanczos convergence (10^{-7} cm^{-1}) for these calculations. As the size of the basis-set is only 4×10^5, the computation time is less than one CPU-hour. The basis-set convergence of absolute vibrational energies is less than 0.05 cm^{-1}, and the ground state anion inversion splitting is converged to 0.01 cm^{-1}. The calculated vibrational frequencies are shown in Table S6.

Table S6: Calculated methyl anion vibrational energies. All values are in cm^{-1}.

		Scaled V_s PES		Unscaled V_o PES		VPT2[a]	
$(\nu_1\nu_2\nu_3^{l3}\nu_4^{l4})^{\pm}$	Γ_{D3h}	CH_3^-	CD_3^-	CH_3^-	CD_3^-	CH_3^-	CD_3^-
$(000^00^0)^+$	A_1'	(4708.4)[b]	(3459.1)[b]	(4755.1)[b]	(3486.3)[b]	(6125.7)[c]	(4513.5)[c]
$(000^00^0)^-$	A_2''	25.0[d]	7.9[e]	11.1[d]	3.3[e]		
$(010^00^0)^+$	A_1'	412.3[f]	335.9[g]	513.5[f]	418.4[g]	600.8	475.3
$(010^00^0)^-$	A_2''	646.1	459.9	684.2	497.8		
$(020^00^0)^+$	A_1'	1007.9	713.8	1058.5	773.2		
$(020^00^0)^-$	A_2''	1403.3	979.3	1438.5	1019.7		
$(000^01^1)^+$	E'	---	---	---	---	1380.3	1015.5
$(000^01^1)^-$	E''	---	---	---	---		
$(030^00^0)^+$	A_1'	1839.0	1279.1	1871.1	1317.4		
$(030^00^0)^-$	A_2''	2307.5	1602.6	2336.3	1637.8		
$(100^00^0)^+$	A_1'	2780.4	2011.1	2779.4	2011.0	2787.8	2117.2
$(100^00^0)^-$	A_2''	2797.4	2015.1	2785.1	2011.6		
$(040^00^0)^+$	A_1'	2809.6	1945.9	2832.0	1980.0		
$(001^10^0)^+$	E'	2876.8	2141.8	2865.4	2136.8	2850.7	2141.2
$(001^10^0)^-$	E''	2886.7	2145.0	2869.0	2137.9		
$(110^00^0)^+$	A_1'	3233.9	2373.4	3365.9	2468.0		
$(040^00^0)^-$	A_2''	3327.6	2313.1	3350.3	2342.9		
$(011^10^0)^+$	E'	3343.5	2525.6	3468.0	2611.1		
$(110^00^0)^-$	A_2''	3421.5	2473.0	3479.2	2521.9		
$(011^10^0)^-$	E''	3510.7	2606.8	3563.2	2651.6		

[a] CCSD(T)/d-aug-pVTZ second order vibrational perturbation theory
[b] 4D zero-point energies
[c] 6D VPT2 zero-point energy
[d] Our experimental value = 21(5) cm^{-1}
[e] Our experimental value = 6(4) cm^{-1}
[f] Our experimental value = 444(13) cm^{-1}
[g] Our experimental value = 373(12) cm^{-1}

Lee *et al.*[17] performed SCF calculations of the CH_3^- harmonic frequencies, which were used by Mitchell *et al.*[18] to assign the transition they observed at 3206.7 cm^{-1} to either of the two CH stretching fundamentals (ν_1 or ν_3). However, we suggest this transition may possibly belong to the $(\nu_1\nu_2) = (00^- \rightarrow 11^+)$ band, the origin of which we calculate to be at 3208.9 cm^{-1} (see Table S6). The agreement of our calculation with the experimental data provides confidence in our calculated FCFs, which may be useful in the determination of autodetachment lifetimes of excited vibrational states of CH_3^-, as was done by Mitchell *et al.*[18]

G. Photoelectron Spectrum Calculation

In order to calculate the reported photoelectron spectra we generated 4D vibrational eigenenergies and wavefunctions on the *ab initio* force field of the neutral $^{\bullet}CH_3$ radical calculated by Schwenke.[19] The 4D energies of the excited out-of-plane bending levels differed

by less than 2 % from the full dimensional energies. The stretching fundamentals differed by less than 0.5 %. Instead of explicit photoelectron cross-section calculations, we scale the overall simulation to match the experimental peak areas.

H. Anion and neutral surface crossing

The intersection between the anion and neutral potential energy surfaces remains an open question. Figure S2 shows the possible seam of intersection between the scaled anion potential surface V_s and the neutral potential surface $V_{radical}$ of Schwenke for different values of ΔE_{elec}. The plot spans the C_{3v} symmetric configuration space ($r_1 = r_2 = r_3$) of our 4D surface and includes the three relevant stationary points: the CH_3^- minimum and transition state and the $^{\bullet}CH_3$ radical minimum. The seam of intersection for a given value of ΔE_{elec} is shown by each labeled contour in the plot. As discussed in the main text, our best *ab initio* estimate of ΔE_{elec} is 415 cm^{-1}. The corresponding seam of intersection between the anion and neutral surfaces is shown as a dashed line in Figure S2. As can be seen, given this ΔE_{elec}, the anion is electronically stable at the anion planar transition state, but unstable at the neutral equilibrium geometry. However, we predict that the uncertainty in the calculated value of ΔE_{elec} is around 100 cm^{-1}, which is enough to move the seam of intersection above or below either of these stationary points. Indeed, the close energy spacing of the anion and neutral adiabatic surfaces over such a large range of geometries suggests that it is inappropriate to consider anion autodetachment by examining the bare adiabatic surfaces without explicitly including the effects of vibrational motion.

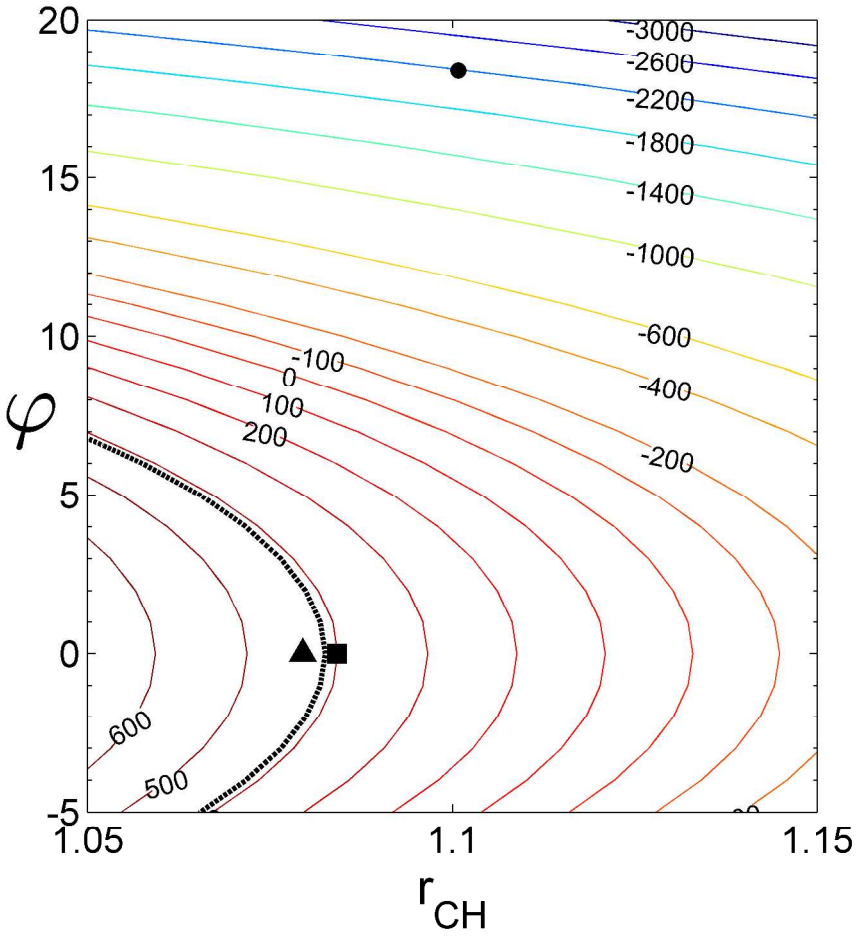

Figure S2: Locations of adiabatic potential energy crossings between the anion and neutral states of $^{\bullet}CH_3$, as a function of the adiabatic electronic contribution to the electron affinity (ΔE_{elec}) and plotted against the umbrella inversion coordinate φ (degrees) and the CH distance. Geometries are constrained to those with C_{3v} symmetry; those of the ground state anion, the planar anion transition state and the ground state neutral denoted with a circle, square and triangle, respectively. The dotted contour shows the crossing location for $\Delta E_{elec} = 415$ cm^{-1}, which is the best estimate obtained in this work. However, it is only above ΔE_{elec} *ca.* 450 cm^{-1} that the extra electron in the anion is bound for all relevant geometries. The energies here are determined from the model potential, described in Subsection E of this appendix.

I. Zero-point energy correction

As determined through theoretical treatment of these systems, approximately half of the EA comes from the difference in zero-point energy (Δ(ZPE)) between the anion and the neutral species, as discussed in Section IV.B in the main text. Table S7 below shows the calculated contribution of the ZPE (Δ(ZPE)) to the electron affinities of $^{\bullet}CH_3$ and $^{\bullet}CD_3$. Adding ΔZPE to ΔE_elec, we obtain 0.094 eV (CH3) and 0.084 eV (CD3) for the electron affinity.

Table S7: Anion and neutral VPT2 ZPEs (all values in cm^{-1}).

	CH_3^-	CD_3^-
CCSD(T)/d-aug-pVTZ	6125.7	4513.5
	$^{\bullet}CH_3$	$^{\bullet}CD_3$
CCSD(T)/d-aug-pVTZ	6471.4	4768.9
Δ(ZPE)	345.7	255.4

J. References

(1) Yamada, C.; Hirota, E.; Kawaguchi, K. *J. Chem. Phys.* **1981**, *75*, 5256.
(2) Hermann, H. W.; Leone, S. R. *J. Chem. Phys.* **1982**, *76*, 4759.
(3) Sears, T. J.; Bunker, P. R.; Davies, P. B.; Johnson, S. A.; Spirko, V. *J. Chem. Phys.* **1985**, *83*, 2676.
(4) Sanov, A.; Grumbling, E. R.; Goebbert, D. J.; Culberson, L. M. *J. Chem. Phys.* **2013**, *138*.
(5) Grumbling, E. R.; Sanov, A. *J. Chem. Phys.* **2011**, *135*, 164302.
(6) Sanov, A. *Annual Review of Physical Chemistry, Vol 65* **2014**, *65*, 341.
(7) Mabbs, R.; Grumbling, E. R.; Pichugin, K.; Sanov, A. *Chem. Soc. Rev.* **2009**, *38*, 2169.
(8) Jacox, M. E. *J. Mol. Spectrosc.* **1977**, *66*, 272.
(9) Cleeton, C. E.; Williams, N. H. *Physical Review* **1934**, *45*, 234.
(10) McKellar, A. R.; Rich, N. H.; Welsh, H. L. *Can. J. Phys.* **1972**, *50*, 1.
(11) Engelking, P. C. *J. Phys. Chem.* **1986**, *90*, 4544.
(12) Ruscic, B. 2013; Vol. 2015.
(13) Pamidimukkala, K. M.; Rogers, D.; Skinner, G. B. *J. Phys. Chem. Ref. Data* **1982**, *11*, 83.
(14) Marquardt, R.; Sagui, K.; Zheng, J. J.; Thiel, W.; Luckhaus, D.; Yurchenko, S.; Mariotti, F.; Quack, M. *J. Phys. Chem. A* **2013**, *117*, 7502.
(15) CFOUR, Coupled-Cluster techniques for Computational Chemistry, a quantum-chemical program package by J.F. Stanton, J. Gauss, M.E. Harding, P.G. Szalay with contributions from A.A. Auer, R.J. Bartlett, U. Benedikt, C. Berger, D.E. Bernholdt, Y.J. Bomble, L. Cheng, O. Christiansen, M. Heckert, O. Heun, C. Huber, T.-C. Jagau, D. Jonsson, J. Jusélius, K. Klein, W.J. Lauderdale, D.A. Matthews, T. Metzroth, L.A. Mück, D.P. O'Neill, D.R. Price, E. Prochnow, C. Puzzarini, K. Ruud, F. Schiffmann, W. Schwalbach, C. Simmons, S. Stopkowicz, A. Tajti, J. Vázquez, F. Wang, J.D. Watts and the integral packages MOLECULE (J. Almlöf and P.R. Taylor), PROPS (P.R. Taylor), ABACUS (T. Helgaker, H.J. Aa. Jensen, P. Jørgensen, and J. Olsen), and ECP routines by A. V. Mitin and C. van Wüllen. For the current version, see http://www.cfour.de.
(16) Wu, K. S.; Simon, H. *Siam Journal on Matrix Analysis and Applications* **2000**, *22*, 602.
(17) Lee, T. J.; Schaefer, H. F. *J. Chem. Phys.* **1985**, *83*, 1784.
(18) Mitchell, S. E.; Conklin, P. M.; Farley, J. W. *J. Chem. Phys.* **2003**, *118*, 11017.
(19) Schwenke, D. W. *Spectrochimica Acta Part a-Molecular and Biomolecular Spectroscopy* **1999**, *55*, 731.